Front. Mater. Sci. 2022, 16(1): 220585
https://doi.org/10.1007/s11706-022-0585-9

RESEARCH ARTICLE

Facile synthesis of Ni-doped SnO_2 nanorods and their high gas sensitivity to isopropanol

Yanqiu YU and Shantang LIU (✉)

Key Laboratory for Green Chemical Process (Ministry of Education), School of Chemistry and Environmental Engineering,
Wuhan Institute of Technology, Wuhan 430073, China

ABSTRACT: In this work, pure SnO_2 and Ni-doped SnO_2 nanorods were synthesized through a one-step template-free hydrothermal method and then used to detect isopropanol. Sensors fabricated with the Ni-doped SnO_2 nanocomposites showed the best gas sensing performance when the Ni doping amount was 1.5 mol.%. The response reached 250 at 225 °C, which was approximately 8.3 times higher than that of the pure SnO_2 nanorods. The limit of detection for isopropanol was as low as 10 ppb at the optimum working temperature. In addition, it also displayed good selectivity and excellent reproducibility. It is believed that the enhanced isopropanol sensing behavior benefit from the increased oxygen defects and larger specific surface area by Ni doping.

KEYWORDS: template-free hydrothermal method; isopropanol; gas sensor; Ni doping; low detection limit

Contents

Received November 18, 2021; accepted December 14, 2021

E-mail: stliu@wit.edu.cn

1 Introduction

Isopropanol is an important volatile organic compound (VOC) that is used to produce ketones, ethers, and esters by oxidation and catalysis. Isopropanol can undergo many reactions with lower alcohols, making it an important chemical intermediate and high-value organic chemical raw material and organic solvent [1]. As a result, isopropanol is widely used as a solvent, disinfectant, pharmaceutical, cosmetic and lubricant [2]. It is also a biomarker in human breath that can be monitored to rapidly screen for diseases such as bile acid diarrhea, liver disease, chronic obstructive pulmonary disease (COPD), and lung cancer [3–4]. However, isopropanol decomposes into toxic gases at high temperatures, which pollute the environment and cause harmful effects on human health [5]. Thus, an effective method is needed to monitor isopropanol.

In the past, gas chromatography and mass spectrometry were common choices for detecting VOCs, but they are limited by high costs, complex manufacturing processes, and the inability to perform *in-situ* and continuous measurements. Fortunately, metal-oxide semiconductor (MOS) gas sensors provide a promising alternative for VOCs monitoring and detection due to their good sensing capabilities and suitability for mass production. Common MOS materials include SnO_2 [6–7], TiO_2 [8–9], ZnO [10–11], In_2O_3 [12–13], CuO [14–15], and Fe_2O_3 [16–17]. Among them, SnO_2 is a typical n-type semiconductor metal oxide with a wide band gap of 3.62 eV that has been widely used to detect many kinds of gases [18].

Although the original SnO_2 nanostructure shows good performance as a gas sensor, it is still limited by defects, such as a high operating temperature and low sensitivity. In recent years, many researchers have prepared SnO_2 materials with new structures to improve their gas-sensing performance. One-dimensional (1D) SnO_2 nanostructures (e.g., wires [19], rods [20], tubes [21] and belts [22]) are promising candidates for highly sensitive gas sensors due to their unique morphology, structure and surface area. Another common technique for enhancing the performance of gas sensors is to introduce dopants. Although noble metal dopants such as Au [23], Ag [24], Pt [25] and Pd [26] greatly improve the gas sensing properties of SnO_2, the high cost restricts their potential practical applications. Thus, it is essential to explore less-expensive alternatives such as common transition metals (e.g., Fe, Co, Ni, and Cu) to reduce the cost while enhancing the sensing performance. Among those alternatives, Ni-doped SnO_2 has been investigated extensively because of its comparable sensing performance to SnO_2 doped with noble metals. Li et al. prepared Ni-doped SnO_2 hollow microspheres by a hydrothermal method, which demonstrated a high sensitivity and selectivity to ethanol [27]. Das et al. used a low-temperature polyol route to synthesize Ni-doped SnO_2 nanoparticles with excellent SO_2 and NO_2 gas sensing performance [28]. Despite these studies, there are few studies on performance improvement for isopropanol gas sensing using Ni-doped SnO_2 nanorods.

In this work, pure SnO_2 and a series of Ni-doped SnO_2 nanorods were synthesized by using a one-step hydrothermal method without a template. The results showed that $Ni_{1.5}$-SnO_2 exhibits better properties than those of the undoped SnO_2 nanorods, including better response to isopropanol, detection limit, and selectivity. The corresponding gas sensing mechanism is also discussed.

2 Experimental

$Na_2SnO_3 \cdot 4H_2O$ was purchased from Sinopharm Chemical Reagent Co., Ltd. (Shanghai, China), and $NiCl_2 \cdot 6H_2O$ was provided by Macklin Biochemical Co., Ltd. (Shanghai, China). All chemical reagents were of analytical grade and were used as received without further purification.

2.1 Materials synthesis

In a typical synthesis, 1 mmol of $Na_2SnO_3 \cdot 4H_2O$ and different amounts of $NiCl_2 \cdot 6H_2O$ were separately dissolved in 80 mL of a mixed solution of ethanol and deionized water (1:1 by volume). The mixture was vigorously stirred for 60 min to obtain a suspension. Then the mixed solution was transferred into a 100 mL Teflon-lined stainless-steel autoclave, and a hydrothermal reaction was carried out at 180 °C for 48 h. After naturally cooling the mixture to room temperature, the products were repeatedly centrifuged several times with deionized water and anhydrous ethanol. The centrifuged products were dried at 80 °C overnight. According to different molar ratios of $n(\mathrm{Ni})/n(\mathrm{SnO_2})$ at 0%, 0.5%, 1.0%, 1.5%, 2.0% and 2.5%, the products were hereafter labeled as SnO_2, $Ni_{0.5}$-SnO_2, $Ni_{1.0}$-SnO_2, $Ni_{1.5}$-SnO_2, $Ni_{2.0}$-SnO_2 and $Ni_{2.5}$-SnO_2, respectively.

2.2 Fabrication and test of the sensor

The structures of the sensor device and the measurement system are identical to those in our previous work [29–30]. Firstly, a certain amount of the prepared material was added to an agate mortar, followed by ethanol. Then, the mixture was mixed and thoroughly ground for 30 min to form a paste. The paste was dropped and spot-coated onto an Al_2O_3 ceramic plate substrate (dimensions of 10 mm × 20 mm × 0.635 mm), onto which a pair of Au interdigitated electrodes (IDEs; width of 0.18 mm and gap width of 0.18 mm) was previously printed. Afterwards, the resulting chip was dried at 60 °C for 2 h, and subsequently annealed at 400 °C for another 2 h. The final sensor was obtained after aging at 200 °C for an additional 24 h. Finally, the gas sensing properties of the sensors were tested by a static measurement system produced by CGS-1TP (Beijing Elite Tech. Co., Ltd., China). The test chamber volume was 18 L. The measurements were performed using a static process in a test chamber with an ambient relative humidity of about 35% and at room temperature (near 25 °C). The gas analyte was injected into the test chamber, and the sensor was placed into the chamber to measure the sensing performance. When the resistance reached a constant value, the upper cover of the test chamber was removed, and the sensor began to recover in air.

In this work, the sensitivity of the sensor was defined as $S = R_a/R_g$ (the reducing gas) or R_g/R_a (the oxidizing gas), where R_a is the resistance of the sensor after stabilizing in the air, and R_g is the resistance after it stabilized when exposed to the target gas. The response and recovery times were defined as the time required for the sensor to reach 90% of the total resistance change when it was exposed to the target gas and to return to 90% of the total resistance when it was re-exposed to air, respectively [31].

2.3 Characterization

The crystalline structure of the samples was characterized by X-ray diffraction (XRD; Bruker, D8 Advance). The morphology and microstructure of the samples was studied by field-emission scanning electron microscopy (FESEM; ZEISS Gemini 300) equipped with an energy-dispersive X-ray spectrometer (EDS). The detailed structure of the prepared samples was further studied using transmission electron microscopy (HRTEM; JEOL JEM 2100F). X-ray photoelectron spectroscopy (XPS; Thermo Fisher, ESCALAB XI) was used to analyze the chemical composition of the products. The specific surface area and the pore size distribution of the samples were determined using a Micromeritics ASAP 2460 specific surface area and porosity analyzer.

3 Results and discussion

3.1 Structure and micromorphology characterization

XRD was used to examine the crystal structure of the hydrothermally synthesized samples with different doping ratios, as shown in Fig. 1(a). Strong and sharp diffraction peaks were observed, which indicate that the samples are highly crystalline. All peaks were assigned to typical tetragonal rutile SnO_2 (JCPDS No. 41-1445) [32]. No peaks of Ni or other crystalline phases were found, probably due to low amounts of the Ni dopant below the detection limit of the XRD or the homogeneous distribution of the dopant. More importantly, even when the Ni concentration was as high as 30 mol.%, all peaks in the XRD pattern of Ni-SnO_2 corresponded to those of tetragonal SnO_2 [33–34]. The diffraction peaks corresponding to (1 1 0) and (1 0 1) crystal planes underwent no shifts (Fig. 1(b)) because Sn^{4+} and Ni^{2+} had the same ionic radius (0.69 Å) [35].

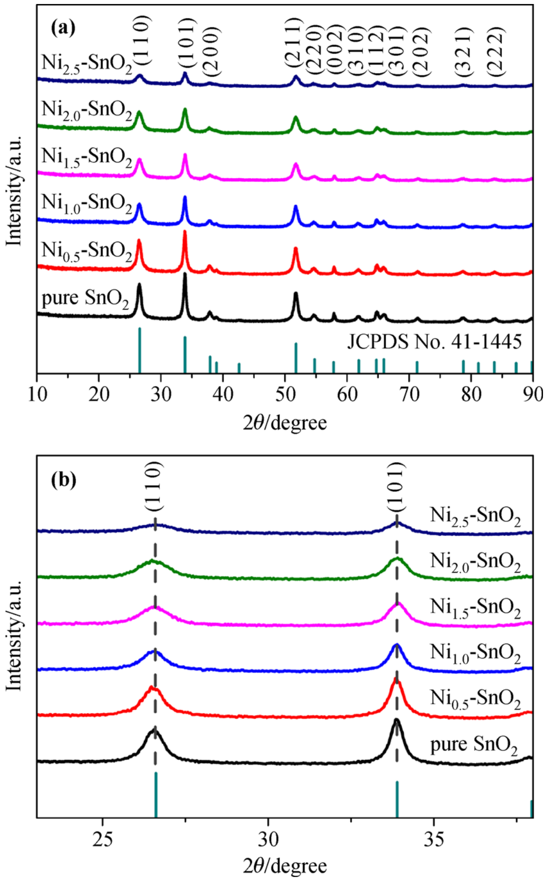

Fig. 1 **(a)** XRD patterns of bare SnO_2 samples with 0 mol.%, 0.5 mol.%, 1.0 mol.%, 1.5 mol.%, 2.0 mol.% and 2.5 mol.% Ni doping. **(b)** High-resolution XRD patterns of (1 1 0) and (1 0 1) peaks for different samples.

The morphology of undoped and 1.5 mol.% doped samples was characterized by SEM images (Fig. 2), demonstrating that both pure SnO_2 and $Ni_{1.5}$-SnO_2 nanorods were stacked on the surface of spheres. Figures 2(b) and 2(d) reveal their respective partially enlarged views. For original SnO_2, well-separated nanocrystalline nanorods were observed (Fig. 2(b)). The sample with a doping ratio of 1.5 mol.% (Fig. 2(d)) had a similar structure to that of pristine SnO_2, but the particles displayed some aggregation. These nanorods were of about 16–20 nm in diameter and 50–80 nm in length. Although the XRD patterns do not show the existence of Ni, the EDS result of the $Ni_{1.5}$-SnO_2 sample confirms its presence (inset of Fig. 2(d)), implying that Ni ions were successfully doped into SnO_2. Then, the inner crystal structures of the

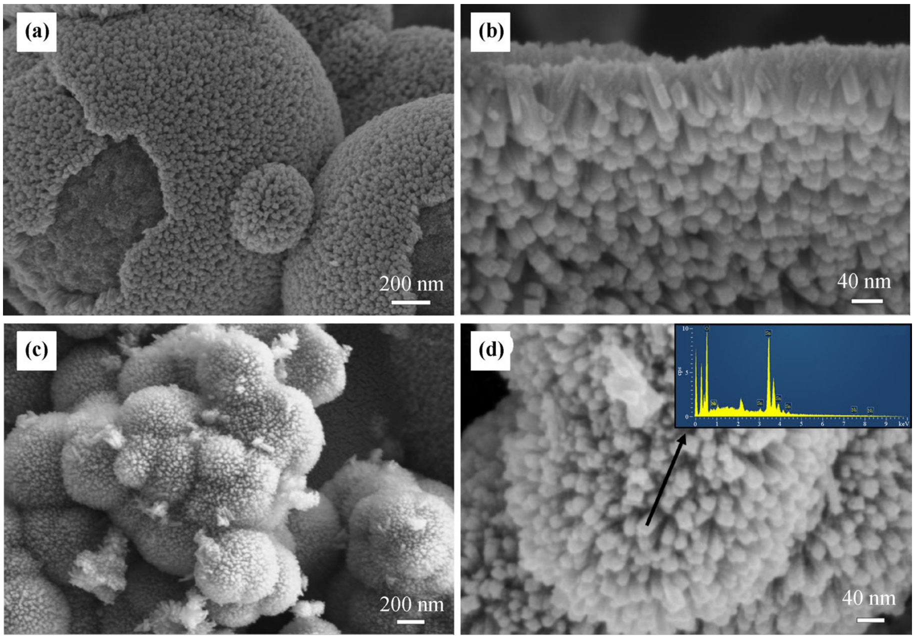

Fig. 2 Typical SEM images of as-obtained nanorods: **(a)(b)** pure SnO_2; **(c)(d)** $Ni_{1.5}$-SnO_2. The inset shows EDX spectrum of $Ni_{1.5}$-SnO_2.

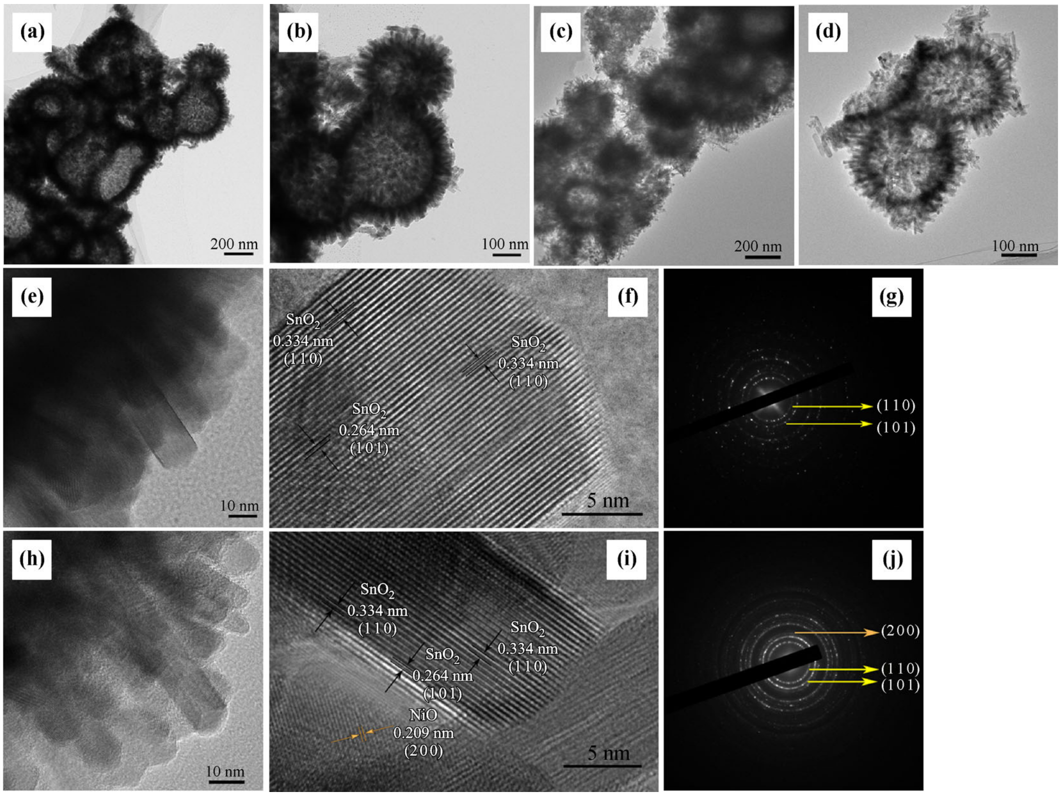

Fig. 3 **(a)(b)(c)(d)** TEM images, **(e)(f)(h)(i)** HRTEM images, and **(g)(j)** SAED patterns of SnO_2 (in panels (a), (b), (e), (f) and (g)) and $Ni_{1.5}$-SnO_2 (in panels (c), (d), (h), (i) and (j)).

synthesized samples were investigated by TEM, as shown in Fig. 3. The morphology was consistent with the SEM observation, and Ni-doped SnO_2 nanorods were more transparent than pure SnO_2 nanorods. The HRTEM observation presented lattice fringes with interplanar spacings of 0.334 and 0.264 nm (Fig. 3(f)), corresponding to (1 1 0) and (1 0 1) planes of rutile SnO_2, respectively, while the interplanar spacing of 0.209 nm was ascribed to the (2 0 0) plane of NiO [27,36] (Fig. 3(i)). The selected area electron diffraction (SAED) analysis showed that the observed diffraction rings or spots belong to (1 1 0) and (1 0 1) planes of SnO_2 and the (2 0 0) plane of NiO.

XPS analysis of the pure SnO_2 and $Ni_{1.5}$-SnO_2 nanorods was conducted to further determine surface chemical compositions and valence states of the products (Fig. 4). All spectra were calibrated to the C 1s peak (284.6 eV). The full-scan spectrum of $Ni_{1.5}$-SnO_2 is shown in Fig. 4(a), which shows that Sn, O, Ni and C existed in the $Ni_{1.5}$-SnO_2 nanorods, and no other element peaks were observed. The C element may be attributed to the sample handling or the absorption of organic molecules prior to XPS measurements; therefore, the $Ni_{1.5}$-SnO_2 nanorods were composed of only Sn, O and Ni. The high-resolution XPS spectrum of Ni 2p is shown in Fig. 4(b). The peaks at 856.04 and 873.37 eV were resolved into Ni $2p_{3/2}$ and Ni $2p_{1/2}$, respectively [37–38]. The Ni $2p_{3/2}$ peaks were assigned to Ni^{2+} ions in $Ni_{1.5}$-SnO_2 [39]. The spin-orbit components ($3d_{3/2}$ and $3d_{5/2}$) of the Sn 3d peak were observed in both pure SnO_2 and $Ni_{1.5}$-SnO_2, as shown in Fig. 4(c). The Sn 3d spectrum contained two peaks located at binding energies of 495.12 and 486.69 eV for pure SnO_2, which were related to the presence of Sn^{4+} in the SnO_2 crystal lattice and correspond to Sn $3d_{3/2}$ and Sn $3d_{5/2}$, respectively. In the Sn 3d survey spectrum of $Ni_{1.5}$-SnO_2, two peaks were observed at binding energies of 494.99 and 486.56 eV, which correspond to Sn $3d_{3/2}$ and Sn $3d_{5/2}$, respectively [40]. The Sn 3d peaks shifted towards a lower binding energy due to the substitution of Sn^{4+} by Ni^{2+}, resulting in increased oxygen defects [35,41]. Figure 4(d) shows the high-resolution O 1s XPS spectra of pure SnO_2 and $Ni_{1.5}$-SnO_2. The low binding energies (530.56 eV for SnO_2 and 530.41 eV for $Ni_{1.5}$-SnO_2) were attributed to the lattice oxygen of SnO_2, while the high binding energies (531.28 eV for SnO_2 and 531.01 eV for $Ni_{1.5}$-SnO_2) were due to chemisorbed oxygen species [36]. The peak areas of the chemisorbed oxygen species belonging to Ni-doped SnO_2 increased.

Information about the specific surface areas and the pore size distributions of SnO_2 nanorods and $Ni_{1.5}$-SnO_2 nanorods were obtained by measuring N_2 adsorption–desorption isotherms (Figs. 5(a) and 5(b)). According to the IUPAC classification, both SnO_2 nanorods and

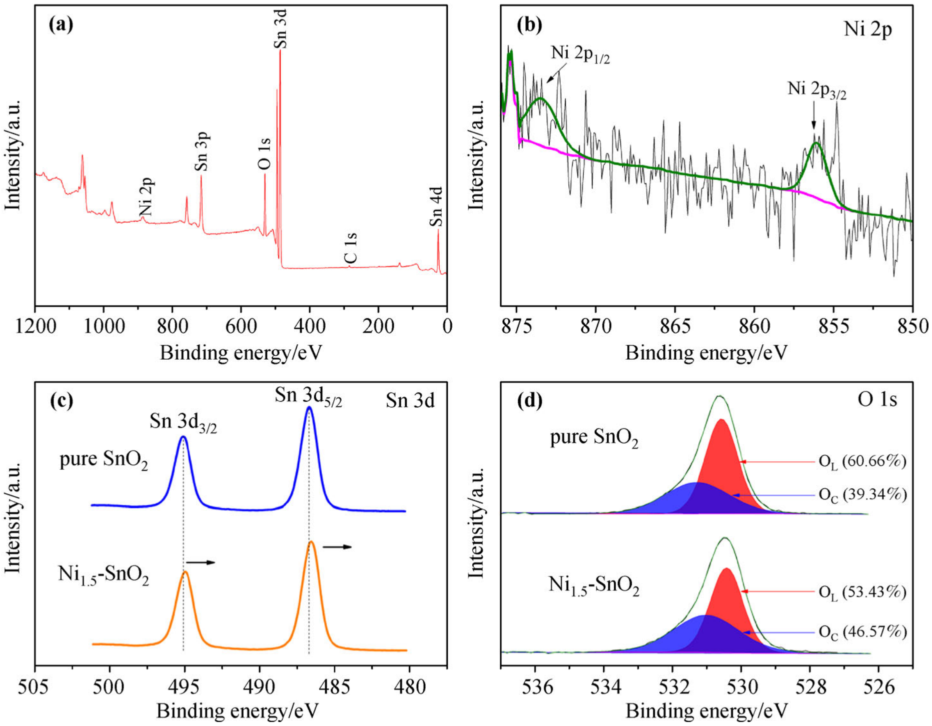

Fig. 4 XPS results: **(a)** full spectrum of $Ni_{1.5}$-SnO_2; **(b)** Ni 2p spectrum of $Ni_{1.5}$-SnO_2; **(c)** Sn 3d spectra of SnO_2 and $Ni_{1.5}$-SnO_2; **(d)** O 1s spectra of SnO_2 and $Ni_{1.5}$-SnO_2.

$Ni_{1.5}$-SnO_2 nanorods exhibited type IV isotherms with a type H3 type hysteresis loop, which indicates the mesoporous material [42–43]. The Brunauer–Emmett–Teller (BET) surface areas of SnO_2 nanorods and $Ni_{1.5}$-SnO_2 nanorods were 40.8575 and 60.8299 $m^2 \cdot g^{-1}$, respectively, after calculations. The increase in the BET surface area may be attributed to a decrease in the grain size. Insets in Fig. 5 showed that the average pore diameters of pure SnO_2 and $Ni_{1.5}$-SnO_2 were 14.9123 and 11.5127 nm, respectively, as calculated from the desorption branch of the N_2 isotherm by the Barrett–Joyner–Halenda (BJH) method. A larger specific surface area is conducive to the gas adsorption and diffusion, which further improves the gas sensing performance [44–45].

3.2 Gas sensing properties to isopropanol

The presence of ionized oxygen species (O_2^-, O^-, or O^{2-}) on the surfaces of semiconductors is closely related to the temperature, which changes the sensor response. Hence, the working temperature with the maximum response value is defined as the optimum working temperature. The temperature–response curve of the samples to 100 ppm (1 ppm = 10^{-6}) isopropanol with different doping ratios is shown in Fig. 6(a). When the operating temperature increased from 150 to 350 °C, the response of all samples first increased and then decreased. These results show that $Ni_{1.5}$-SnO_2 showed better gas sensing performance at 225 °C for 100 ppm isopropanol than samples with other doping ratios. For example, the sensor based on $Ni_{1.5}$-SnO_2 had the highest response among all sensors, whose response reached 250 at 225 °C, which is 8.3 times higher than that of the undoped sample. The resistance change curves of the sensors to 100 ppm isopropanol gas at 225 °C are represented in Fig. 7(b). All sensors exhibited typical n-type gas-sensing behavior, and Ni-doped SnO_2 exhibited a higher resistance in air and a lower resistance in isopropanol compared with pure SnO_2. This should be favorable for enhancing the response to the reducing gases (R_a/R_g).

The dynamic response–recovery characteristics of as-obtained sensors toward various concentrations of isopropanol vapor were tested at the optimal operating temperature to measure the current detection ability. Figure 7(a) shows the dynamic response–recovery curves

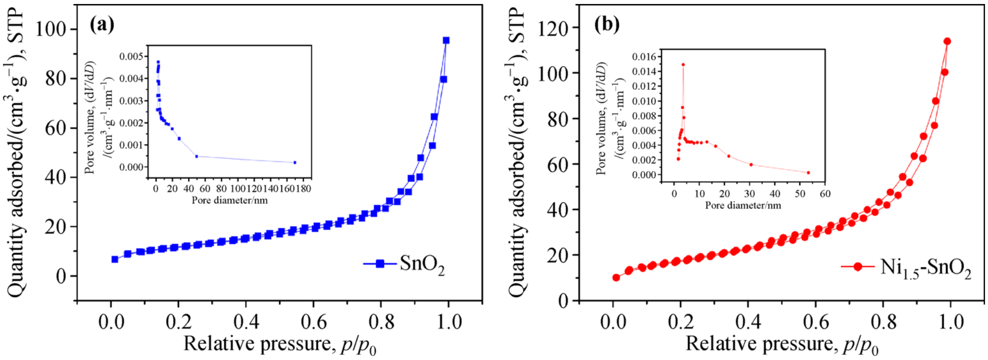

Fig. 5 N_2 adsorption–desorption isotherms and corresponding pore-size distributions of **(a)** pure SnO_2 and **(b)** $Ni_{1.5}$-SnO_2 samples.

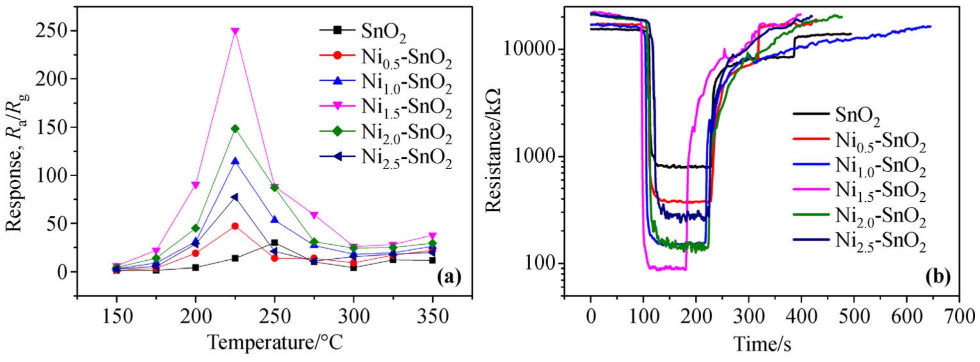

Fig. 6 **(a)** Temperature–response curves for samples of pure SnO_2, $Ni_{0.5}$-SnO_2, $Ni_{1.0}$-SnO_2, $Ni_{1.5}$-SnO_2, $Ni_{2.0}$-SnO_2, and $Ni_{2.5}$-SnO_2 to 100 ppm isopropanol. **(b)** Dynamic resistance curves of pure SnO_2, $Ni_{0.5}$-SnO_2, $Ni_{1.0}$-SnO_2, $Ni_{1.5}$-SnO_2, $Ni_{2.0}$-SnO_2, and $Ni_{2.5}$-SnO_2 to 100 ppm isopropanol at 225 °C.

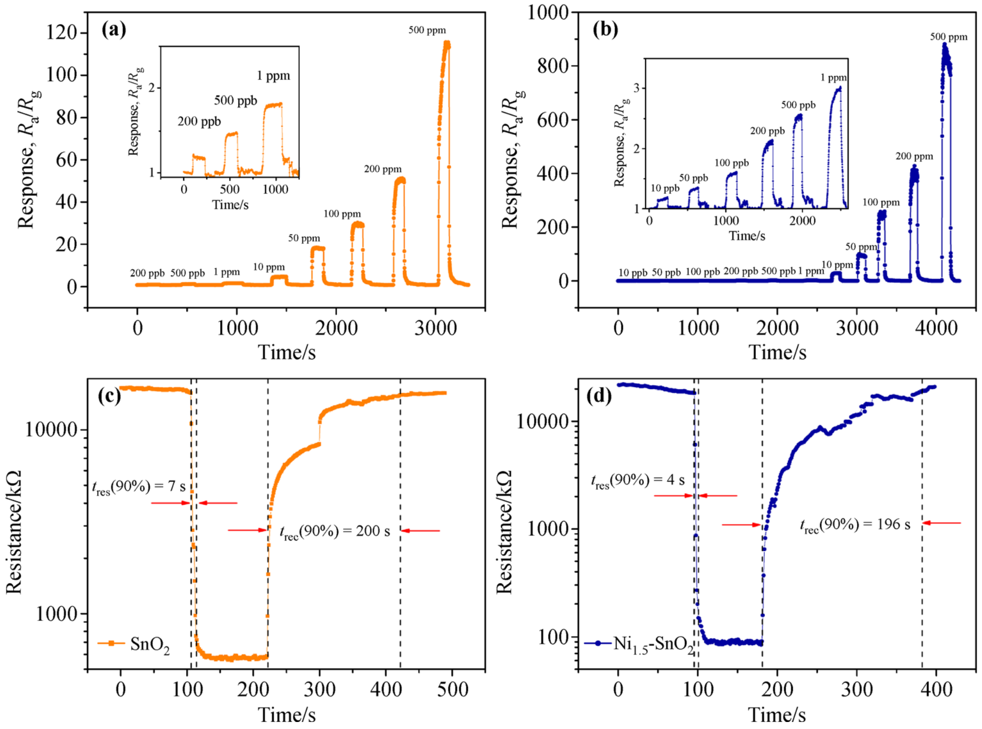

Fig. 7 Response–recovery curves of **(a)** pure SnO_2 and **(b)** $Ni_{1.5}$-SnO_2 sensors to isopropanol with the increasing concentration at their respective optimal operating temperatures. Response–recovery curves of **(c)** pure SnO_2 and **(d)** $Ni_{1.5}$-SnO_2 sensors to 100 ppm isopropanol at the optimal operating temperatures.

of the pure SnO_2 sensor with an isopropanol concentration range from 200 ppb (1 ppb = 10^{-9}) to 500 ppm. The inset shows the dynamic response-recovery curves with an isopropanol concentration range from 200 ppb to 1 ppm. Figure 7(b) shows the dynamic response–recovery curves of the $Ni_{1.5}$-SnO_2 sensor with an isopropanol concentration range from 10 ppb to 500 ppm. The inset shows dynamic response–recovery curves with an isopropanol concentration range from 10 ppb to 1 ppm. The $Ni_{1.5}$-SnO_2 sensor showed a greatly enhanced detection limit and response to isopropanol. Furthermore, the detection limit of the $Ni_{1.5}$-SnO_2 sensor was as low as 10 ppb, which is about 1.16. The response-recovery time of the sensors were explored next. According to the definitions of the response time and recovery time, we calculated the response-recovery time of SnO_2 and $Ni_{1.5}$-SnO_2 sensors, and the results are shown in Figs. 7(c) and 7(d). Values of the corresponding response–recovery time were 7/200 s and 4/196 s towards 100 ppm isopropanol at their optimal temperatures. The response and recovery times were very similar.

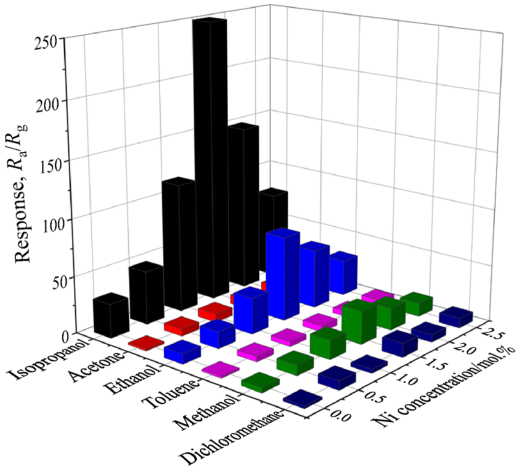

Fig. 8 The response of SnO_2, $Ni_{0.5}$-SnO_2, $Ni_{1.0}$-SnO_2, $Ni_{1.5}$-SnO_2, $Ni_{2.0}$-SnO_2, and $Ni_{2.5}$-SnO_2 sensors toward various 100 ppm test gases at the optimal operating temperatures.

Figure 8 shows the selectivity of the sensors to 100 ppm of different VOC vapors (isopropanol, acetone, ethanol, toluene, methanol, and dichloromethane) at the optimum operating temperature. The sensors' response to isopropanol was better than that to other VOC vapors, indicating that they have good selectivity to isopropanol.

To survey the reproducibility of the sensor response, six reversible response–recovery cycles for the $Ni_{1.5}$-SnO_2 sensor to 100 ppm isopropanol vapor are displayed in Fig. 9. After six testing cycles, the sensors had only small fluctuations and maintained a high response (about 250), which indicates their good reversibility.

The stability reflects the service life of a sensor. To

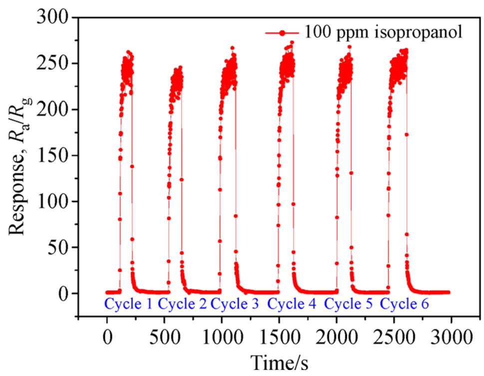

Fig. 9 Cyclic response curve of the sensor based on $Ni_{1.5}$-SnO_2 to 100 ppm isopropanol at the optimal operating temperature.

determine stability data of the $Ni_{1.5}$-SnO_2 sensor, 100 ppm of isopropanol was tested for 15 d at the optimal operating temperature, and the results are shown in Fig. 10. The response did not significantly change, indicating that the sensors were stable, further demonstrating their potential application prospects.

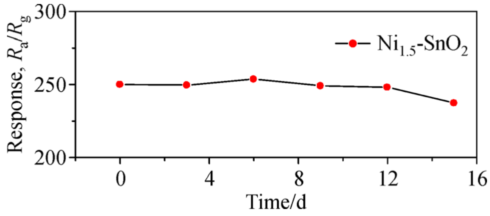

Fig. 10 Long-term stability of the $Ni_{1.5}$-SnO_2 sensor to 100 ppm isopropanol at the optimal operating temperature.

Table 1 compares the isopropanol sensing performance in this work and previously reported literature [5,46–53]. The $Ni_{1.5}$-SnO_2 based sensor displayed an ultra-low detection limit and high response.

3.3 Gas-sensing mechanism of Ni-SnO_2

The gas sensing mechanism of SnO_2 gas sensors is surface-controlled, and the gas sensing performance is primarily determined by the species and the chemisorbed oxygen density on the surface of SnO_2 [54]. When a pristine SnO_2 gas sensor is exposed to air, oxygen molecules are adsorbed on the active sites of SnO_2 nanorods to generate chemisorbed oxygen species (O_2^-, O^-, and O^{2-}) by trapping electrons from the SnO_2 conduction band to generate a potential barrier, which increases the resistance. When SnO_2 nanorods are exposed to a reducing gas such as isopropanol, the chemisorbed oxygen anions on the surface of SnO_2 react with isopropanol gas. The gas removes chemisorbed oxygen anions and is oxidized. As a result, these free electrons trapped by chemisorbed oxygen species are released and return to conduction band of SnO_2, which decreases the resistance. The relevant reaction equations are [46,50]:

$$O_2 + e^- \longleftrightarrow O_2^- \tag{1}$$

$$O_2^- + e^- \longleftrightarrow 2O^- \tag{2}$$

$$O^- + e^- \longleftrightarrow O^{2-} \tag{3}$$

$$(CH_3)_2CHOH + 9O^{2-} \longleftrightarrow 3CO_2 + 4H_2O + 18e^- \tag{4}$$

For Ni-doped SnO_2, the increased gas sensing performance may be due to an increase in the oxygen deficiencies when Sn^{4+} ions in the lattice were substituted by Ni^{2+}. This is in close agreement with the XPS result. The above reaction can be written as [27,55]:

$$NiO \xrightarrow{SnO_2} Ni_{Sn}'' + O_O^{\times} + V_O^{\bullet\bullet} \tag{5}$$

where Ni_{Sn}'' is the Ni–Sn substitutional site with double negative charge, $V_O^{\bullet\bullet}$ is the oxygen vacancy, and $O_O^{\times}$ is the neutral oxygen site. From the defect reaction shown in Eq. (5), there is an increase in the number of oxygen vacancies in Ni-doped SnO_2 samples, and oxygen molecules in the atmosphere tend to adsorb onto these

Table 1 Performance comparison of gas-sensing characteristics on various sensing materials toward isopropanol

Material	Concentration/ppm	Temperature/°C	Response	Detection limit/ppm	Ref.
Pt-SnO_2 nanosheets	100	220	190.50	5	[5]
SnO_2/ZnO core/shell composites	500	300	103.3	1	[46]
SnO_2 nanorings	100	250	7.27	1	[47]
CuO–SnO_2 nanorods	100	280	50.4	20	[48]
g-C_3N_4/SnO_2 composites	100	200	61.63	1	[49]
SnO_2 nanorods	200	325	19.29	20	[50]
Sm-SnO_2 nanoarrays	100	251	43	1	[51]
Double-shelled SnO_2 tubes	100	180	14.5	5	[52]
Pt-SnO_2 nanoflowers	100	250	171	1	[53]
Ni-SnO_2 nanorods	100	225	250	0.01	this work

oxygen vacancies; thus, the number of chemisorbed oxygen species (O_2^-, O^-, and O^{2-}) of $Ni_{1.5}$-SnO_2 increased compared with pure SnO_2, in agreement with the XPS results. In addition, a thicker electron depletion layer near the SnO_2 surface formed due to the presence of more defective oxygen vacancies, leading to a reduced background electron concentration, which facilitated electron transfer from gas molecules to the conduction band. This produces a much larger change in resistance [55], as shown in Fig. 6(b); therefore, the substitutional doping of Ni in SnO_2 changes the defect equilibrium of the gas sensor and facilitates the adsorption of O_2 on the surface of SnO_2 [56]. Secondly, Ni^{2+} dopant ions also acted as catalytic sites that facilitated the oxidation of analyte gases [57]. In addition to these, the introduction of Ni dopant increased the surface area of the nanorods, which was verified in the BET analysis test. This provides more adsorption sites for reducing gases when the composite has a larger surface area [58]. The basic isopropanol gas sensing mechanisms of pure SnO_2 and Ni-doped SnO_2-based sensors are depicted in Fig. 11.

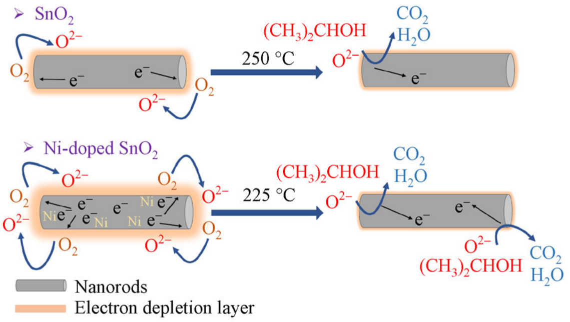

Fig. 11 Schematic diagrams of sensors based on SnO_2 nanorods and Ni-doped SnO_2 nanorods when exposed to isopropanol.

4 Conclusions

In this paper, pure SnO_2 nanorods and a series of Ni-SnO_2 nanorods with different Ni doping amounts were synthesized through a one-step template-free hydrothermal method. The experimental results showed that the $Ni_{1.5}$-SnO_2 based sensor exhibited a high response, high selectivity, low detection limit, and outstanding repeatability to isopropanol at 225 °C. The excellent gas sensing properties of this material were mainly attributed to increased oxygen defects and larger specific surface area caused by the Ni doping. The sensor based on $Ni_{1.5}$-SnO_2 provides a high-performance isopropanol gas sensor with many potential application prospects.

Acknowledgements This work was supported by the 12th Graduate Innovative Fund of Wuhan Institute of Technology (Grant No. CX2020269).

References

[1] Cai X, Hu D, Deng S, et al. Isopropanol sensing properties of coral-like ZnO–CdO composites by flash preparation via self-sustained decomposition of metalorganic complexes. Sensors and Actuators B: Chemical, 2014, 198: 402–410

[2] Hu D, Han B, Deng S, et al. Novel mixed phase SnO_2 nanorods assembled with SnO_2 nanocrystals for enhancing gas-sensing performance toward isopropanol gas. The Journal of Physical Chemistry C, 2014, 118(18): 9832–9840

[3] Chien P J, Suzuki T, Tsujii M, et al. Bio-sniffer (gas-phase biosensor) with secondary alcohol dehydrogenase (S-ADH) for determination of isopropanol in exhaled air as a potential volatile biomarker. Biosensors & Bioelectronics, 2017, 91: 341–346

[4] Jiang L, Wang C, Wang J, et al. Ultrathin $BiVO_4$ nanosheets sensing electrode for isopropanol sensor based on pyrochlore-$Gd_2Zr_2O_7$ solid state electrolyte. Sensors and Actuators B: Chemical, 2020, 321: 128478

[5] Dong C, Liu X, Xiao X, et al. Combustion synthesis of porous Pt-functionalized SnO_2 sheets for isopropanol gas detection with a significant enhancement in response. Journal of Materials Chemistry A: Materials for Energy and Sustainability, 2014, 2(47): 20089–20095

[6] Acharyya S, Jana B, Nag S, et al. Single resistive sensor for selective detection of multiple VOCs employing SnO_2 hollow-spheres and machine learning algorithm: a proof of concept. Sensors and Actuators B: Chemical, 2020, 321: 128484

[7] Kim J H, Kim J Y, Lee J H, et al. Indium-implantation-induced enhancement of gas sensing behaviors of SnO_2 nanowires by the formation of homo-core–shell structure. Sensors and Actuators B: Chemical, 2020, 321: 128475

[8] Haidry A A, Xie L, Wang Z, et al. Hydrogen sensing and adsorption kinetics on ordered mesoporous anatase TiO_2 surface. Applied Surface Science, 2020, 500: 144219

[9] Kang Y, Kim K, Cho B, et al. Highly sensitive detection of benzene, toluene, and xylene based on CoPP-functionalized TiO_2 nanoparticles with low power consumption. ACS Sensors, 2020, 5(3): 754–763

[10] Zhu L, Li Y, Zeng W. Hydrothermal synthesis of hierarchical flower-like ZnO nanostructure and its enhanced ethanol gas-sensing properties. Applied Surface Science, 2018, 427: 281–287

[11] Chen Y, Zhang Y, Zhang H, et al. Design and evaluation of Cu-modified ZnO microspheres as a high performance formaldehyde sensor based on density functional theory. Applied Surface Science, 2020, 532: 147446

[12] Tao Z, Li Y, Zhang B, et al. Bi-doped urchin-like In_2O_3 hollow

spheres: synthesis and improved gas sensing and visible-light photocatalytic properties. Sensors and Actuators B: Chemical, 2020, 321: 128623

[13] Jun L, Chen Q, Fu W, et al. Electrospun Yb-doped In_2O_3 nanofiber field-effect transistors for highly sensitive ethanol sensors. ACS Applied Materials & Interfaces, 2020, 12(34): 38425–38434

[14] Sisman O, Zappa D, Bolli E, et al. Influence of iron and nitrogen ion beam exposure on the gas sensing properties of CuO nanowires. Sensors and Actuators B: Chemical, 2020, 321: 128579

[15] Mnethu O, Nkosi S S, Kortidis I, et al. Ultra-sensitive and selective p-xylene gas sensor at low operating temperature utilizing Zn doped CuO nanoplatelets: insignificant vestiges of oxygen vacancies. Journal of Colloid and Interface Science, 2020, 576: 364–375

[16] Cao Z, Jiang Z, Cao L, et al. Lattice expansion and oxygen vacancy of α-Fe_2O_3 during gas sensing. Talanta, 2021, 221: 121616

[17] Zhai C, Liu Y, Du L, et al. Novel malonic acid assisted synthesized porous Fe_2O_3 microspheres for ultra-fast response and recovery toward triethylamine. New Journal of Chemistry, 2020, 44(15): 5929–5936

[18] Zhang Y, Wang C, Zhao L, et al. Preparation of Ce-doped SnO_2 cuboids with enhanced 2-butanone sensing performance. Sensors and Actuators B: Chemical, 2021, 341: 130039

[19] Kwak C H, Woo H S, Lee J H. Selective trimethylamine sensors using Cr_2O_3-decorated SnO_2 nanowires. Sensors and Actuators B: Chemical, 2014, 204: 231–238

[20] Wang H, Chen M, Rong Q, et al. Ultrasensitive xylene gas sensor based on flower-like SnO_2/Co_3O_4 nanorods composites prepared by facile two-step synthesis method. Nanotechnology, 2020, 31(25): 255501

[21] Shan H, Liu C, Liu L, et al. Excellent toluene sensing properties of SnO_2–Fe_2O_3 interconnected nanotubes. ACS Applied Materials & Interfaces, 2013, 5(13): 6376–6380

[22] Yang T, Gu K, Zhu M, et al. ZnO–SnO_2 heterojunction nanobelts: synthesis and ultraviolet light irradiation to improve the triethylamine sensing properties. Sensors and Actuators B: Chemical, 2019, 279: 410–417

[23] Liu Y, Li X, Wang Y, et al. Hydrothermal synthesis of Au@SnO_2 hierarchical hollow microspheres for ethanol detection. Sensors and Actuators B: Chemical, 2020, 319: 128299

[24] Choi S W, Katoch A, Sun G J, et al. NO_2-sensing performance of SnO_2 microrods by functionalization of Ag nanoparticles. Journal of Materials Chemistry C: Materials for Optical and Electronic Devices, 2013, 1(16): 2834–2841

[25] Xue D, Wang P, Zhang Z, et al. Enhanced methane sensing property of flower-like SnO_2 doped by Pt nanoparticles: a combined experimental and first-principle study. Sensors and Actuators B: Chemical, 2019, 296: 126710

[26] Cai Z, Park S. Synthesis of Pd nanoparticle-decorated SnO_2 nanowires and determination of the optimum quantity of Pd nanoparticles for highly sensitive and selective hydrogen gas sensor. Sensors and Actuators B: Chemical, 2020, 322: 128651

[27] Li Z, Yi J. Enhanced ethanol sensing of Ni-doped SnO_2 hollow spheres synthesized by a one-pot hydrothermal method. Sensors and Actuators B: Chemical, 2017, 243: 96–103

[28] Das S, Girija K G, Debnath A K, et al. Enhanced NO_2 and SO_2 sensor response under ambient conditions by polyol synthesized Ni doped SnO_2 nanoparticles. Journal of Alloys and Compounds, 2021, 854: 157276

[29] Xiao L, Shu S, Liu S. A facile synthesis of Pd-doped SnO_2 hollow microcubes with enhanced sensing performance. Sensors and Actuators B: Chemical, 2015, 221: 20–126

[30] Shu S, Wang M, Wei Y, et al. Synthesis of surface layered hierarchical octahedral-like structured Zn_2SnO_4/SnO_2 with excellent sensing properties toward HCHO. Sensors and Actuators B: Chemical, 2017, 243: 1171–1180

[31] Bi W, Wang W, Liu S. Synthesis of Rh-SnO_2 nanosheets and ultra-high triethylamine sensing performance. Journal of Alloys and Compounds, 2020, 817: 152730

[32] Xiao L, Xu S, Yu G, et al. Efficient hierarchical mixed Pd/SnO_2 porous architecture deposited microheater for low power ethanol gas sensor. Sensors and Actuators B: Chemical, 2018, 255: 2002–2010

[33] Castro R H R, Hidalgo P, Muccillo R, et al. Microstructure and structure of NiO–SnO_2 and Fe_2O_3–SnO_2 systems. Applied Surface Science, 2003, 214(1–4): 172–177

[34] Lin Z, Li N, Chen Z, et al. The effect of Ni doping concentration on the gas sensing properties of Ni doped SnO_2. Sensors and Actuators B: Chemical, 2017, 239: 501–510

[35] Hu J, Wang T, Wang Y, et al. Enhanced formaldehyde detection based on Ni doping of SnO_2 nanoparticles by one-step synthesis. Sensors and Actuators B: Chemical, 2018, 263: 120–128

[36] Meng D, Liu D Y, Wang G S, et al. Low-temperature formaldehyde gas sensors based on NiO–SnO_2 heterojunction microflowers assembled by thin porous nanosheets. Sensors and Actuators B: Chemical, 2018, 273: 418–428

[37] Liu X, Zhang J, Guo X, et al. Enhanced sensor response of Ni-doped SnO_2 hollow spheres. Sensors and Actuators B: Chemical, 2011, 152(2): 162–167

[38] Wang Y, Xiong G, Liu X, et al. Structure and reducibility of NiO–MoO_3/γ-Al_2O_3 catalysts: effects of loading and molar ratio. The Journal of Physical Chemistry C, 2008, 112(44): 17265–17271

[39] Wang Z, Li Z, Sun J, et al. Improved hydrogen monitoring

properties based on p-NiO/n-SnO_2 heterojunction composite nanofibers. The Journal of Physical Chemistry C, 2010, 114(13): 6100–6105

[40] Zhao B, Guo X, Zhao W, et al. Yolk–shell Ni@SnO_2 composites with a designable interspace to improve the electromagnetic wave absorption properties. ACS Applied Materials & Interfaces, 2016, 8(42): 28917–28925

[41] Xu S, Gao J, Wang L, et al. Role of the heterojunctions in In_2O_3-composite SnO_2 nanorod sensors and their remarkable gas-sensing performance for NO_x at room temperature. Nanoscale, 2015, 7(35): 14643–14651

[42] Lu J, Xie Y, Luo F, et al. Heterostructures of mesoporous hollow Zn_2SnO_4/SnO_2 microboxes for high-performance acetone sensors. Journal of Alloys and Compounds, 2020, 844: 155788

[43] Zhu Z, Zheng L, Zheng S, et al. Multichannel pathway-enriched mesoporous NiO nanocuboids for the highly sensitive and selective detection of 3-hydroxy-2-butanone biomarkers. Journal of Materials Chemistry A: Materials for Energy and Sustainability, 2019, 7(17): 10456–10463

[44] Wang J, Hu C, Xia Y, et al. Mesoporous ZnO nanosheets with rich surface oxygen vacancies for UV-activated methane gas sensing at room temperature. Sensors and Actuators B: Chemical, 2021, 333: 129547

[45] Qin S, Tang P, Feng Y, et al. Novel ultrathin mesoporous ZnO–SnO_2 n–n heterojunction nanosheets with high sensitivity to ethanol. Sensors and Actuators B: Chemical, 2020, 309: 127801

[46] Poloju M, Jayababu N, Manikandan E, et al. Enhancement of the isopropanol gas sensing performance of SnO_2/ZnO core/shell nanocomposites. Journal of Materials Chemistry C: Materials for Optical and Electronic Devices, 2017, 5(10): 2662–2668

[47] Li S H, Chu Z, Meng F F, et al. Highly sensitive gas sensor based on SnO_2 nanorings for detection of isopropanol. Journal of Alloys and Compounds, 2016, 688: 712–717

[48] Zhang B, Fu W, Meng X, et al. Synthesis of actinomorphic flower-like SnO_2 nanorods decorated with CuO nanoparticles and their improved isopropanol sensing properties. Applied Surface Science, 2018, 456: 586–593

[49] Zhao R, Wang Z, Zou T, et al. Synthesis and enhanced sensing performance of g-C_3N_4/SnO_2 composites toward isopropanol. Chemistry Letters, 2018, 47(7): 881–882

[50] Hu D, Han B, Han R, et al. SnO_2 nanorods based sensing material as an isopropanol vapor sensor. New Journal of Chemistry, 2014, 38(6): 2443–2450

[51] Zhao Y, Li Y, Wan W, et al. Surface defect and gas-sensing performance of the well-aligned Sm-doped SnO_2 nanoarrays. Materials Letters, 2018, 218: 22–26

[52] Sun H, Zhang C, Peng Y, et al. Synthesis of double-shelled SnO_2 hollow cubes for superior isopropanol sensing performance. New Journal of Chemistry, 2019, 43(12): 4721–4726

[53] Bi W, Xiao W, Liu S. Synthesis of Pt-doped SnO_2 flower-like hierarchical structure and its gas sensing properties to isopropanol. Journal of Materials Science, 2021, 56(10): 6095–6109

[54] Wang Y, Zhao Z, Sun Y, et al. Fabrication and gas sensing properties of Au-loaded SnO_2 composite nanoparticles for highly sensitive hydrogen detection. Sensors and Actuators B: Chemical, 2017, 240: 664–673

[55] Singkammo S, Wisitsoraat A, Sriprachuabwong C, et al. Electrolytically exfoliated graphene-loaded flame-made Ni-doped SnO_2 composite film for acetone sensing. ACS Applied Materials & Interfaces, 2015, 7(5): 3077–3092

[56] Sun P, Zhou X, Wang C, et al. One-step synthesis and gas sensing properties of hierarchical Cd-doped SnO_2 nanostructures. Sensors and Actuators B: Chemical, 2014, 190: 32–39

[57] Zhou Q, Chen W, Xu L, et al. Highly sensitive carbon monoxide (CO) gas sensors based on Ni and Zn doped SnO_2 nanomaterials. Ceramics International, 2018, 44(4): 4392–4399

[58] Song Z, Chen W, Zhang H, et al. Highly sensitive and selective acetylene sensors based on p–n heterojunction of NiO nanoparticles on flower-like ZnO structures. Ceramics International, 2019, 45(16): 19635–19643